First-principles theory of the Dirac semimetal Cd$_3$As$_2$ under Zeeman magnetic field

Santu Baidya and David Vanderbilt[*]

Department of Physics & Astronomy, Rutgers University, Piscataway, New Jersey 08854, USA

Time-reversal broken Weyl semimetals have attracted much attention recently, but certain aspects of their behavior, including the evolution of their Fermi surface topology and anomalous Hall conductivity with Fermi-level position, have remained underexplored. A promising route to obtain such materials may be to start with a nonmagnetic Dirac semimetal and break time-reversal symmetry via magnetic doping or magnetic proximity. Here we explore this scenario in the case of the Dirac semimetal Cd$_3$As$_2$ based on first-principles density-functional calculations and subsequent low-energy modeling of Cd$_3$As$_2$ in the presence of a Zeeman field applied along the symmetry axis. We clarify how each fourfold degenerate Dirac node splits into four Weyl nodes, two with chirality ± 1 and two higher-order nodes with chirality ± 2. Using a minimal $k \cdot p$ model Hamiltonian whose parameters are fit to the first-principles calculations, we detail the evolution of the Fermi surfaces and their Chern numbers as the Fermi energy is scanned across the region of the Weyl nodes at fixed Zeeman field. We also compute the intrinsic anomalous Hall conductivity as a function of the Fermi-level position, finding a characteristic inverted-dome structure. Cd$_3$As$_2$ is especially well suited to such a study because of its high mobility, but the qualitative behavior revealed here should be applicable to other Dirac semimetals as well.

I. INTRODUCTION

The compound Cd$_3$As$_2$ has been widely studied in recent years for its three-dimensional graphenelike characteristics [1–6]. The existence of three-dimensional Dirac cones at the Fermi level in this compound has attracted much attention in the field of topological semimetals, as the only Dirac semimetals observed experimentally to date are Cd$_3$As$_2$ [7] and Na$_3$Bi [8,9]. Cd$_3$As$_2$ has many interesting properties in addition to the existence of the Dirac cone, such as an abnormally large g factor of around 20 [10], which still demands microscopic understanding. Most of the interest in the past few years has focused on the Dirac crossing, which is protected by the crystalline C_{4v} symmetry.

Starting from a Dirac Hamiltonian, a Weyl semimetal phase [11] can be reached by breaking either inversion symmetry or time-reversal (TR) symmetry [12]. TR symmetry can be broken by doping with magnetic ions, by proximity effects near an interface to a magnetic material, or by application of an external magnetic field.

In the first two cases, the TR breaking is most naturally represented in terms of an effective Zeeman field acting on the spins, while the last also brings in orbital effects. A previous study of the Dirac semimetal Na$_3$Bi and its evolution into a Weyl semimetal phase under Zeeman field has been discussed using tight-binding methods in Ref. [13], but this material may not be an optimal choice for such a study in view of its chemical instability.

Regarding orbital effects in Cd$_3$As$_2$, the quantum Hall effect in a nanoplate of thickness $50 - 100$ nm has been experimentally reported and attributed to Weyl orbit formation [14]. Thus, the appearance and evolution of the Weyl nodes in Dirac materials with TR-broken perturbations is a topic of pressing interest.

In this paper, we focus on the effects of a Zeeman field on the nodal structure, Fermi-surface configuration, and anomalous Hall conductivity of Cd$_3$As$_2$. Our work is motivated in part by a recent proposal [15,16] that a Dirac semimetal could be a platform for the realization of unconventional superconductivity in a TR-broken Weyl semimetal [16] resulting from the presence of magnetic dopants or proximity to a magnetic substrate or overlayer.

We start from realistic first-principles density functional theory (DFT) calculations in which a Zeeman field is applied along the symmetry axis, and then construct a linearized $k \cdot p$ model to describe the low-energy physics near the Dirac point. While elementary discussions often describe the TR-symmetry breaking as resulting in a splitting of the Dirac node into a pair of Weyl nodes, we clarify that four Weyl nodes appear instead. For a given strength of Zeeman field, we give a detailed description of the evolution of the Fermi surfaces of the electron and hole pockets and their nontrivial Chern numbers as the Fermi level E_F is tuned over the range of energies where the Weyl points occur. We also compute and track the anomalous Hall conductivity, paying special attention to its behavior as E_F passes through the Weyl node positions, predicting a characteristic signature that we suggest as a target of future experimental observation.

II. ELECTRONIC STRUCTURE OF Cd$_3$As$_2$ UNDER ZEEMAN FIELD

A. First-principles calculations

Figure 1(a) shows the crystal structure of the Cd$_3$As$_2$, corresponding to a defective antifluorite structure. The com-
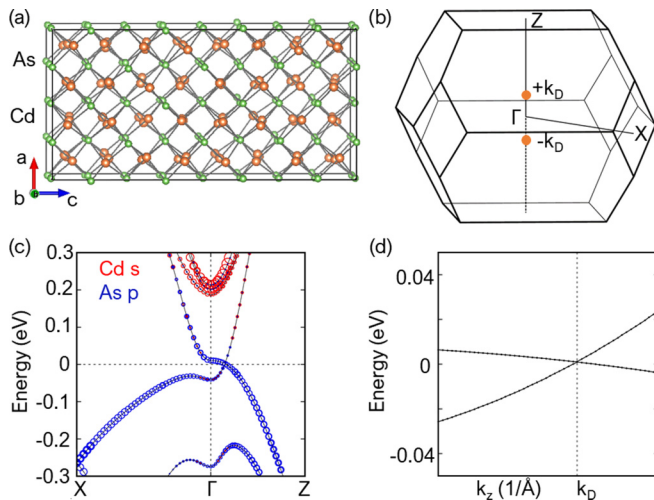
FIG. 1. (a) Conventional unit cell of Cd_3As_2 with space group $I4_1/acd$. (b) Brillouin zone of the primitive unit cell with position of Dirac points. (c) Cd s (red circles) and As p (blue circles) character projected onto the energy manifold under nonmagnetic PBE+SOC approximation. (d) PBE+SOC band structure with linear Dirac crossing at the Fermi level.

FIG. 2. (a) Nonmagnetic PBE+SOC band structure of crossing Dirac bands along the $\Gamma - Z$ direction. (b) Same but along $X' - \Gamma' - X'$ at $k_z = k_D$, i.e., passing through the Dirac point. (c), (d) Same as (a), (b) but under a Zeeman field of $h = 100$ T along the [001] direction. Inset of (c) shows four Weyl nodes labeled as w_1 through w_4.

pound has an intermediate-temperature phase above 475 °C with space group $P4_2/nmc$ [1] having 40 atoms in the primitive cell. A high-temperature $Fm\bar{3}m$ antifluorite phase has also been reported above 600 °C. There has been confusion in the literature about the low-temperature phase that occurs below 475 °C [7,17,18]. A previous work identified the low-temperature phase as a noncentrosymmetric $I4_1cd$ structure [17,18], and subsequent theoretical tight-binding calculations were carried out on this structure to propose a possible TR-symmetric Weyl semimetal phase with broken inversion symmetry [3]. However, recent experiments [7] clarify that this phase is indeed centrosymmetric, with space group $I4_1/acd$ containing 80 atoms per primitive cell. We focus on the latter structure here. The conventional 160-atom cell is shown in Fig. 1, and consists of eight layers of Cd atoms and eight layers of As atoms stacked along the c axis. The structure can be regarded as an antifluorite structure with 25% vacancies on the Cd sites, with each As atom having six Cd nearest neighbors.

DFT calculations are carried out in a full-potential linear augmented plane wave framework as implemented in the WIEN2K package [19]. The Perdew-Burke-Ernzerhof (PBE) exchange-correlation functional [20] is employed. Spin-orbit coupling (SOC) is taken into account using the second-order variational approach implemented in the WIEN2K package.

The PBE band structure in Fig. 1(c) shows the nonmagnetic band structure near the Fermi level. All bands are doubly degenerate because of the presence of inversion and TR symmetry. Two of these degenerate bands cross each other at a Dirac point (fourfold degeneracy) protected by C_4 symmetry at $k_z = +k_D$ on the Γ-Z path along the k_z axis. The Cd s and As p orbital projections shown in Fig. 1(c) indicate that the crossing occurs between an s band with positive slope and a p band with negative slope. By symmetry, there will be another Dirac point at $k_z = (0, 0, -k_D)$ as shown in Fig. 1(b). The
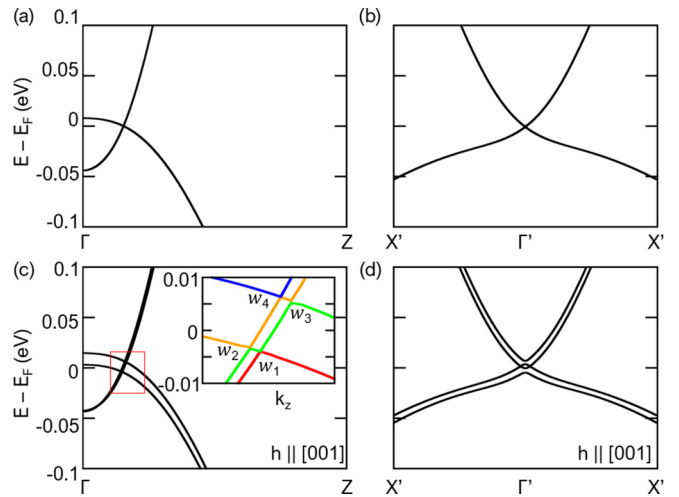
zoomed view in Fig. 1(d) shows the crossing point along the positive k_z axis.

To study the Weyl semimetal phase of Cd_3As_2, we calculate the band structure under an effective Zeeman field introduced to represent the effect of doping with magnetic impurities at a mean-field level. This is similar to the spirit of previous works such as the study of the quantum anomalous Hall effect in Cr-doped topological insulator films of Bi_2Te_3 [21,22]. We anticipate collinear easy-axis ferromagnetic order and thus apply the field along the $\hat{z}$ symmetry axis. While our theory treats the effective Zeeman field h as a free parameter, we have chosen to present our results for $h = 100$ T, corresponding to a splitting of 11.6 meV for a free electron, which could be a reasonable spin-exchange field achievable by magnetic doping. Orbital magnetic effects, such as those that give rise to magnetoresistance oscillations, are not considered in our theory.

The effect of the Zeeman field on the band structure of the Dirac semimetal is presented in Fig. 2. For reference, Fig. 2(a) shows the band dispersion along the Γ–Z symmetry axis in the absence of the Zeeman field. The Dirac crossing occurs at $k_z = k_D = 0.037$ Å^{-1}, and by definition at zero energy. Henceforth we also reset the origin of k_z to coincide with the Dirac point location k_D, so subsequently k_z is always measured relative to k_D. The dispersions of the two crossing bands are roughly quadratic relative to Γ, but show a linear crossing character when attention is focused sufficiently close to k_D.

Figure 2(b) shows the corresponding band structure plotted along a straight line passing through the Dirac point and parallel to X–Γ–X (hence labeled (X'–Γ'–X'). The crossing is clearly linear sufficiently close to the Dirac point at the center, with quadratic and higher variations further from Γ'. By contrast, for the smaller $P4_2/nmc$ unit cell proposed previously [1], we find that the corresponding curve has almost no linear

component, with quadratic and higher behaviors dominating even very close to the Dirac point.

Figures 2(c) and 2(d) show the corresponding results in the presence of the effective Zeeman field of $h = 100\,\text{T}$ along the z axis. The Kramers-degenerate bands are now all split by the Zeeman field. Along the Γ–Z direction shown in Fig. 2(c), the crossing bands belong to different irreducible representations of the C_4^z rotation operator, so there is no avoided crossing. Instead, each of the four crossings generates a Weyl node. The structure in the vicinity of these crossings is shown in the inset of Fig. 2(c), where the four crossing bands are shown in red, green, orange, and blue in order of increasing energy. The four Weyl nodes generated from the crossings are labeled as w_j, with w_1 connecting the bottom two bands, w_2 and w_3 connecting the middle bands, and w_4 connecting the top two bands. Figure 2(d) shows the dispersion on the same X'–Γ'–X' line as in Fig. 2(b); this line does not pass exactly through any of the Weyl points, so the states are all nondegenerate at Γ'. The dispersion looks like two copies of Fig. 2(b), slightly shifted in energy by the Zeeman perturbation, and with each

showing an avoided crossings at Γ' because of the influence of SOC. The details of the structure in the vicinity of the avoided crossings in Fig. 2(d) will become clearer in the context of the effective $k \cdot p$ model that we introduce next.

B. Effective $k \cdot p$ Hamiltonian

To understand the behavior of this system and compute its anomalous Hall conductivity for Fermi level positions in the vicinity of the Weyl nodes, it is useful to introduce a minimal effective $k \cdot p$ model for the bands in this region. Following the work of Wang *et al.* [3,8], our effective Hamiltonian is written in the basis of spin-orbit coupled states $|S_{1/2}, J_z = 1/2\rangle$, $|P_{3/2}, J_z = 3/2\rangle$, $|S_{1/2}, J_z = -1/2\rangle$, and $|P_{3/2}, J_z = -3/2\rangle$, where s and p states reside on Cd and As atoms, respectively. After defining $\mathbf{k}$ relative to the Dirac point at $(0, 0, k_\text{D})$, expanding in powers of $\mathbf{k}$, and keeping the leading terms allowed by symmetry, the Hamiltonian takes the form

$$H(\mathbf{k}) = \begin{pmatrix} v_s k_z + \beta_s h & A k_+ & 0 & G k_-^2 \\ A k_- & -v_p k_z + \beta_p h & G k_-^2 & 0 \\ 0 & G k_+^2 & v_s k_z - \beta_s h & -A k_- \\ G k_+^2 & 0 & -A k_+ & -v_p k_z - \beta_p h \end{pmatrix}. \tag{1}$$

The terms involving v_s, v_p, and A describe a slightly tilted Dirac cone with perfectly linear dispersion, where v_s and v_p are the magnitudes of the Fermi velocities for the s and p bands, respectively, and A determines the Fermi velocity in the k_x and k_y directions, where $k_\pm = k_x \pm i k_y$. Parameters β_s and β_p represent the effect of the Zeeman exchange field h on the two sets of states. Quadratic terms involving k_z^2 and $k_x^2 + k_y^2$ have been omitted on the grounds that they will not be important when working in a small region of $(\mathbf{k}, E)$ space close to the Dirac point, and because they do not induce any Berry curvature.

By contrast, we have included the quadratic terms involving $G k_+^2$ and $G k_-^2$. These represent SOC and have important qualitative and quantitative effects on the nature of the Fermi surfaces and the anomalous Hall response. Without these terms, the upper-left and lower-right 2×2 blocks of $H(\mathbf{k})$ (the spin-up and spin-down sectors) would be completely uncoupled, leading to the existence of nodal loops where spin-up and spin-down Fermi surfaces intersect. Wieder *et al.* [23] pointed out [see their Supp. Eq. (237)] that the fourfold rotational symmetry actually allows the $G k_+^2$ and $G k_-^2$ terms to be generalized to $G k_-^2 + G' k_+^2$ and $G k_+^2 + G' k_-^2$, respectively, with $G' \ll G$. The inequality arises because G', unlike G, would vanish in the presence of continuous rotational symmetry and is only induced by an additional weak crystal field perturbation. We therefore neglect the G' term in this paper.

The parameters A, G, v_s, v_p, β_s, and β_p are computed from the PBE+SOC band structure calculations to make our microscopic model Hamiltonian close to the realistic picture. The parameter A is taken from the slope of the bands at the

Dirac crossing plotted in the (k_x, k_y) plane at $k_z = k_\text{D}$ in the absence of an external field, as shown in the Fig. 2(b). The parameters v_s and v_p are given by the slopes of the Cd s and As p bands at their crossing point, as in Fig. 2(a). The parameters β_s and β_p describe the linear dependence of the exchange splittings of the Cd s and As p bands on the strength of the Zeeman field h, as determined by the band splittings very close to the Weyl nodes.

The prefactor G of the off-diagonal k_+^2 and k_-^2 terms is obtained from a close inspection of the bands near $E = E_\text{F}$ in Fig. 2(d), where a tiny gap (not visible in the figure) arises at each crossing between the second and third bands. In the absence of G, the spin-up and spin-down sectors would become completely decoupled, Eq. (1) would become block diagonal, and these avoided crossings would disappear. Thus, a nonzero G is required for a qualitatively correct description. However, the determination of G is rather sensitive to details of the first-principles band structure, so we later allow it to vary to study how these avoided crossings affect the anomalous Hall conductivity.

The parameter values obtained as described above from the first-principles calculations are $A = 0.99\,\text{eV-Å}$, $v_s = 2.68\,\text{eV-Å}$, $v_p = 0.56\,\text{eV-Å}$, $\beta_s = 0.054\,\text{meV/T}$, $\beta_p = 0.115\,\text{meV/T}$, and $G = 10\,\text{eV-Å}^2$. The last three were obtained from calculations at $h = 100\,\text{T}$, but their values are not sensitive to variations of h in this range.

C. Chirality and Chern numbers of Fermi pockets

The $k \cdot p$ model described above allows for a convenient description of the locations of the Weyl points, the shapes of
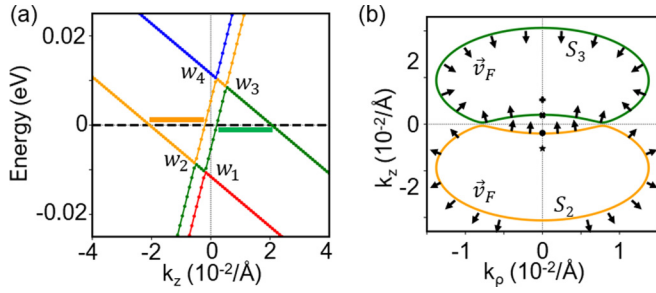
FIG. 3. (a) Dispersion of the four Dirac-derived bands along the k_z axis within the $k \cdot p$ model. Bands are colored red, green, orange, and blue in order of increasing energy; Weyl points w_1, w_2, w_3, and w_4 are marked. (b) Electron pocket in third band (orange) and hole pocket in second band (green) for $E_F = 0$, as indicated by horizontal orange and green lines in (a). Weyl point positions are shown by dots on the k_z axis.

the Fermi surfaces, and the behavior of the anomalous Hall conductivity in the vicinity of the Dirac crossing.

As discussed earlier and illustrated in the inset of Fig. 2(c), the single Dirac crossing in the absence of Zeeman field produces a set of four Weyl points on the k_z axis in the presence of the field. Within our $k \cdot p$ model, the bands are exactly linear along the k_z axis as illustrated in Fig. 3(a), and the locations $k_{z,j}$ of the Weyl points $w_1 \dots w_4$ are

$$
\begin{aligned}
k_{z,1} &= -(\beta_p - \beta_s)h/(v_s + v_p), \\
k_{z,2} &= -(\beta_s + \beta_p)h/(v_s + v_p), \\
k_{z,3} &= (\beta_s + \beta_p)h/(v_s + v_p), \\
k_{z,4} &= (\beta_p - \beta_s)h/(v_s + v_p).
\end{aligned}
\tag{2}
$$

The corresponding chiralities are $\chi_1 = -1$, $\chi_2 = -2$, $\chi_3 = +2$, and $\chi_4 = +1$, as obtained analytically [24–26] from the model Hamiltonian. Our sign convention is such that a Weyl node of positive chirality is a source and sink of Berry curvature in the conduction and valence bands, respectively [27]. This is the opposite sign convention from that adopted in Ref. [28] and some other works. As a reminder, w_1 connects the bottom two bands, w_2 and w_3 connect the middle bands, and w_4 connects the top two bands of the four-band group. With our model parameters, Weyl points w_1 and w_4 occur at $k_z = \mp 1.9 \times 10^{-3}$ Å^{-1} and $E = \mp 10.5$ meV, and w_2 and w_3 occur at $k_z = \mp 5.2 \times 10^{-3}$ Å^{-1} and $E = \mp 8.6$ meV.

Next, we vary the Fermi level over the energy range of the Weyl points and study the evolution of the Fermi surfaces. For this purpose it is convenient to transform to cylindrical (k_ρ, k_ϕ, k_z) coordinates, with $k_\rho^2 = k_x^2 + k_y^2$ and $k_\phi = \tan^{-1}(k_y/k_x)$. The symmetry of Eq. (1) is such that $E(\mathbf{k}) = E(k_\rho, k_z)$ independent of k_ϕ, so all Fermi surfaces have cylindrical symmetry within this model, and it is convenient to plot Fermi surfaces in (k_ρ, k_z) space. For example, Fig. 3(b) shows the Fermi surfaces for the case $E_F = 0$, the nominal charge neutrality point. (The full 3D Fermi surface would be obtained by rotating this figure about the k_x axis.) Referring back to Fig. 3(a), it is clear that the orange Fermi surface is an electron pocket surrounding occupied Weyl point w_2, while the green one is a hole pocket surrounding unoccupied Weyl node w_3. The small gap separating the orange
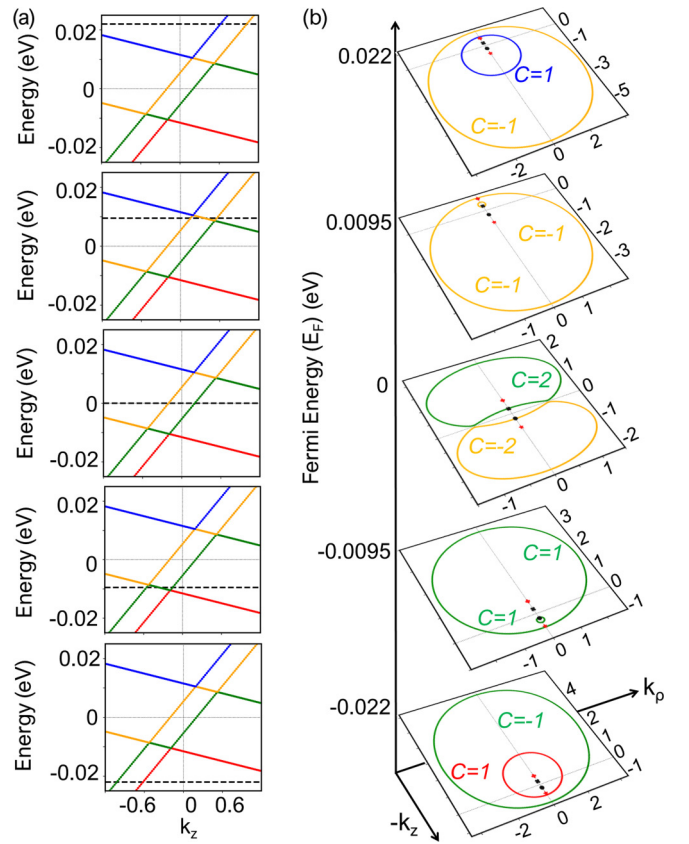
FIG. 4. (a) Band structure showing several Fermi-level positions (dashed lines) as E_F is tuned across the energy range of the Weyl nodes. (b) Contours of Fermi surfaces projected on the (k_z, k_ρ) plane corresponding to each Fermi-level position, for $G = 10 \, \mathrm{eV} \mathrm{Å}^2$, with k_z and k_ρ in units of $10^{-2} \mathrm{Å}^{-1}$. Chern numbers of electron and hole pockets are indicated.

and green Fermi surfaces in Fig. 3(b) is a consequence of the nonzero G parameter in our model. Corresponding figures for a range of Fermi energies spanning over the range of Weyl points are shown in Fig. 4.

The Chern number C_n of a Fermi pocket band in band n is obtained by calculating the Berry flux passing through its Fermi surface [29,30] according to

$$
C_n = \frac{1}{2\pi} \oint_{S_F} d^2k \, \Omega_n(\mathbf{k}),
\tag{3}
$$

where

$$
\Omega_n = \mathbf{\Omega_n} \cdot \hat{\mathbf{v}}_F
\tag{4}
$$

is the surface-normal component of the Berry curvature. Note the sign convention: $\hat{\mathbf{v}}_F$ is the Fermi velocity unit vector, which is outward-directed for electron pockets and inward for hole pockets as illustrated in Fig. 3(a). The Berry curvature components in tensor notation ($\Omega_{\alpha\beta} = \epsilon_{\alpha\beta\gamma}\Omega_\gamma$) are computed using the Kubo formula

$$
\Omega_{\alpha\beta,n} = 2\mathrm{Im} \sum_{m \neq n} \frac{\langle n|v_\alpha|m\rangle \langle m|v_\beta|n\rangle}{(E_n - E_m)^2},
\tag{5}
$$

where $v_\alpha = \partial H / \partial k_\alpha$ are the velocity operators. In practice, we carry out the calculation in cylindrical coordinates, computing

Ω_z from matrix elements of v_ρ, v_ϕ, and Ω_ρ from matrix elements of v_ϕ and v_z. To evaluate Eq. (4), we need to combine these as $\Omega = (\Omega_\rho v_{F,\rho} + \Omega_z v_{F,z})/|\mathbf{v}_F|$. Then the Fermi surface integral is carried out by discretizing each (k_ρ, k_z) path describing a Fermi surface, such as the green curve in Fig. 3(a). We then compute the needed ingredients at each (k_ρ, k_z) point along the path and sum, taking account of phase space details such as the 2π coming from the k_ϕ integral. We have checked that the results are always very close to integer values as long as the discrete sampling is sufficiently dense.

The resulting Fermi surface Chern numbers are shown for a range of Fermi level positions in Fig. 4. The Fermi level positions are indicated by black dashed lines in Fig. 4(a) and the corresponding Fermi surfaces projected onto the $k_\rho - k_z$ plane are shown in Fig. 4(b).

Starting from the top of Fig. 4, where the Fermi level crosses only the blue and orange bands, the Chern numbers are $+1$ and -1 for these bands, respectively. This is consistent with Gosálbez-Martínez *et al.* [28], where the Chern number C_n of a Fermi surface in band n was shown to be equal to the sum of chiralities of the enclosed Weyl points connecting to band $n - 1$ minus the corresponding sum for touchings with band $n + 1$. For the blue band, there is only a single contribution of the first type, coming from w_4 with $\chi_4 = +1$, giving $C_4 = +1$. For the orange band, w_2 and w_3 contribute positively and w_4 contributes negatively, giving $C_3 = (-2) + (+2) - (+1) = -1$.

The remaining panels of Fig. 4 show the evolution of the Fermi surfaces as the Fermi energy is swept through the region of the Weyl points. We find topologically nontrivial Fermi pockets in all cases, suggesting that Cd$_3$As$_2$ may be a promising material for realizing unconventional superconductivity based on topological Fermi surfaces in a Weyl semimetal [15,16]. When the Fermi level is at the nominal charge neutrality level of $E_F = 0$, we find electron (orange) and hole (green) pockets with Chern numbers ∓ 2, respectively. The effect of the finite $G = 10$ eVÅ^2 makes a small separation between these pockets, as shown in Fig. 4(b), with a separation that grows larger as G is increased. In the next section, we investigate the effect of varying this parameter on the Berry curvature and anomalous Hall conductivity of the system.

D. Berry curvature

As we shall see, the parameter G in the $k \cdot p$ Hamiltonian plays an important role in producing Berry curvature and influencing the anomalous Hall conductivity. However, even when $G = 0$, Berry curvature is present. In this case, the separation between the electron and hole pockets in Fig. 4(b) for E_F near zero vanishes. In this case, the spin-up and spin-down sectors of Eq. (1) do not mix, and their ellipsoidal Fermi surfaces intersect without any avoided crossing. Nevertheless, there is still a nonzero Berry curvature, since Weyl points w_1 and w_4 are still present and serve as equal and opposite sources of Berry flux in the two spin sectors. The fact that these are offset from one another along
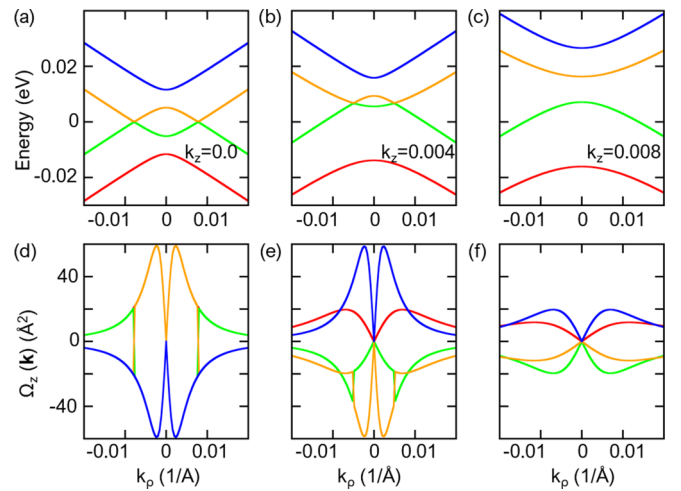
FIG. 5. (a)–(c) Band structure plotted versus k_ρ for three different values of k_z when G is zero. (d)–(f) Berry curvature of the corresponding bands, color-coded accordingly.

the k_z axis allows for a nonzero net anomalous Hall conductivity.

Figures 5(a)–(c) show the band structure plotted versus k_ρ for three values of k_z. At the critical value $k_z = k_{z,3} = 0.0052$ Å (not shown), the second and third bands have a quadratic touching; this will become the location of Weyl point w_3, but with $G = 0$ it is still part of a surface of degeneracy between the second and third bands. The corresponding Berry curvature of the bands is plotted in Figs. 5(d)–5(f).

Turning on a finite G causes a mixing of the spin-up and spin-down sectors, so crossings between bands associated with these sectors are gapped almost everywhere. The exceptions are the locations of the quadratic Weyl points w_2 and w_3, which survive the arrival of the finite G. Because G multiplies k_+^2 and k_-^2 terms in Eq. (1), it is responsible for the higher-order ($\chi = \pm 2$) nature of these Weyl points. The band structures are shown in Figs. 6(a)–6(c) for a G value of
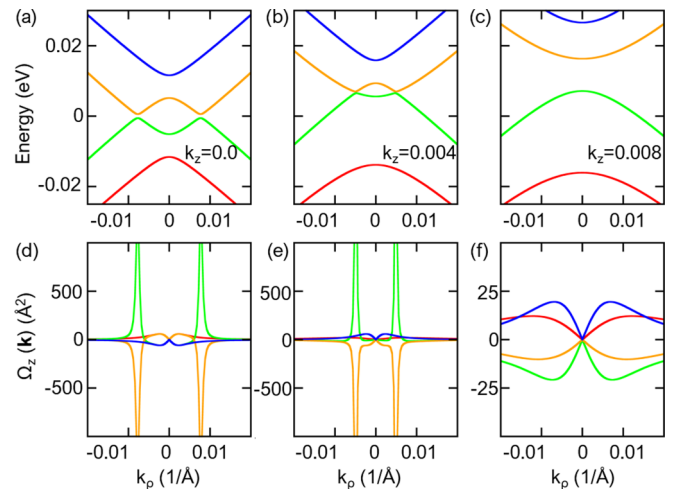
FIG. 6. (a)–(c) Band structure plotted versus k_ρ for three different values of k_z when G is 10 eVÅ^2. (d)–(f) Berry curvature of the corresponding bands, color coded accordingly.

$10\,\mathrm{eV\AA}^2$. There are now small avoided crossings between the second and third bands in Figs. 6(a) and 6(b). Figures 6(d)–6(f) show the corresponding Berry curvature on these bands, showing very large peaks near the avoided crossings, with the potential to make large contributions to the anomalous Hall conductivity.

E. Anomalous Hall conductivity

Once the TR symmetry is broken by the presence of the Zeeman field, a nonzero Hall conductivity $\sigma_{yx}^{\mathrm{AHC}}$ is expected on symmetry grounds. We refer to this as anomalous Hall conductivity since we have in mind that the magnetic order has its origin in magnetic impurities or proximity effects. We note in passing that Hall conductivity measurements have been reported for Cd_3As_2 nanoplates [14,31]. Here we report the behavior of the intrinsic anomalous Hall conductivity as a function of Fermi-level position in the context of our $k \cdot p$ model of bulk Cd_3As_2. In doing so, we neglect extrinsic defect scattering mechanisms, which could play a role experimentally, especially when magnetism is introduced by magnetic dopants. We expect these contributions to be relatively featureless as a function of Fermi level position, and in any case they are beyond the scope of the present paper.

To calculate the intrinsic anomalous Hall conductivity, we have adopted the Fermi-surface integral approach of Refs. [29,30]. In this formulation,

$$\sigma_{\alpha\beta} = \frac{-e^2}{\hbar}\frac{1}{2\pi^2}\sum_{n\gamma}\epsilon_{\alpha\beta\gamma}K_{n\gamma}\,, \qquad (6)$$

where

$$K_{n\gamma} = \frac{1}{2\pi}\oint_{S_F} d^2k\,\Omega_n\,k_\gamma \qquad (7)$$

measures the surface-normal Berry flux passing through the Fermi surface, as in Eq. (3), but now weighted by the wave-vector component k_γ. As the z component of the intrinsic anomalous Hall conductivity (i.e., $\sigma_{yx}^{\mathrm{AHC}}$) is the only one allowed by symmetry, we compute K_{nz} for each band n and for each point on the Fermi surface and integrate, as described previously below Eq. (5) for the earlier Chern-number calculation.

The resulting anomalous Hall conductivity is plotted as a function of Fermi-level position for several values of the G parameter in Fig. 7, again for our reference Zeeman field of $h=100$ T. The analysis above applies to the split Dirac cone located on the positive k_z axis, but there is an equal contribution coming from the inversion image on the negative k_z axis (inversion does not reverse the sign of the anomalous Hall conductivity), giving an additional factor of 2 that has been included in the results presented in Fig. 7.

When $G = 0$, we find a result that is nonzero but constant as a function of Fermi level position. Further investigations shows that the spin-up and spin-down contributions are both perfectly linear in E_F, as expected for tilted Weyl cones, but the slopes are equal and opposite so that the sum is constant. However, these contributions do not simply cancel; the constant residual can be understood as coming from the
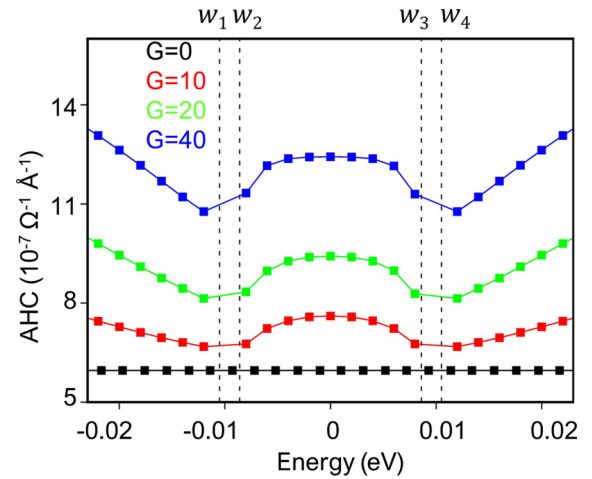
FIG. 7. Anomalous Hall conductivity $\sigma_{yx}^{\mathrm{AHC}}$ plotted versus Fermi level position for several values of the G parameter. Energies of the Weyl nodes are indicated by the vertical dashed lines.

off-centering along k_z of the spin-up and spin-down Weyl cones.

Turning now to the results for nonzero G, we find that an additional contribution to the anomalous Hall conductivity grows in with increasing G. This contribution follows an interesting pattern in which there is an inverted dome in the energy region between the upper and lower pairs of Weyl nodes, a relatively smaller contribution near those nodes, and then a further growth that is roughly linear in $|E_F|$ in the energy range outside the nodes. We have varied the effective Zeeman field value from 100 T to 400 T and obtained a qualitatively similar behavior. This distinctive behavior of the anomalous Hall conductivity could serve as a fingerprint of a material with a Zeeman-split Dirac cone if it can be observed experimentally, as by transport measurements of a gated thin film.

III. SUMMARY AND CONCLUSIONS

Motivated to understand the effect of magnetic order arising from magnetic doping or proximity in the Dirac semimetal Cd_3As_2, we have presented a detailed investigation of the splitting of the Dirac node into Weyl nodes in the presence of a TR-breaking Zeeman field oriented along the symmetry axis. We emphasize that the Dirac node does not simply split into a pair of Weyl nodes with chirality ± 1 as is commonly expected. Instead, we find two nodes of chirality ± 2 connecting the nominal valence and conduction bands, in addition to nodes of chirality ± 1 connecting lower and higher pairs of bands. Starting from first-principles density-functional calculations and fitting a $k \cdot p$ model that is well suited to explore the low-energy physics, we analyze the evolution of the Fermi surfaces, their Chern numbers, and their contributions to the anomalous Hall conductivity, as a function of Fermi level position using the $k \cdot p$ model. The behavior of the anomalous Hall conductivity shows a distinctive pattern that may be a suitable target for experimental confirmation. The presence of multiple, topologically nontrivial electron and hole

pockets for Fermi energies near charge neutrality suggests possible avenues for the realization of novel forms of superconducting pairing. Finally, we anticipate that the methods presented here can find use more generally in unraveling the intriguing physics of TR symmetry breaking in Dirac semimetals.

[1] M. v. Stackelberg and R. Paulu, Untersuchungen an den Phosphiden und Arseniden des Zinks und Cadmiums. Das Zn_3P_2-Gitter, Z. Phys. Chem. B **28**, 427 (1935).

[2] I. Crassee, R. Sankar, W.-L. Lee, A. Akrap, and M. Orlita, 3D Dirac semimetal Cd_3As_2: A review of material properties, Phys. Rev. Mater. **2**, 120302 (2018).

[3] Zhijun Wang, Hongming Weng, Quansheng Wu, Xi Dai, and Zhong Fang, Three-dimensional Dirac semimetal and quantum transport in Cd_3As_2, Phys. Rev. B **88**, 125427 (2013).

[4] Z. K. Liu, J. Jiang, B. Zhou, Z. J. Wang, Y. Zhang, H. M. Weng, D. Prabhakaran, S.-K. Mo, H. Peng, P. Dudin, T. Kim, M. Hoesch, Z. Fang, X. Dai, Z. X. Shen, D. L. Feng, Z. Hussain, and Y. L. Chen, A stable three-dimensional topological Dirac semimetal Cd_3As_2, Nat. Mater. **13**, 677 (2014).

[5] S. Jeon, B. B. Zhou, A. Gyenis, B. E. Feldman, I. Kimchi, A. C. Potter, Q. D. Gibson, R. J. Cava, A. Vishwanath, and A. Yazdani, Landau quantization and quasiparticle interference in the three-dimensional dirac semimetal Cd_3As_2, Nat. Mater. **13**, 851 (2014).

[6] S. Borisenko, Q. Gibson, D. Evtushinsky, V. Zabolotnyy, B. Büchner, and R. J. Cava, Experimental Realization of a Three-Dimensional Dirac Semimetal, Phys. Rev. Lett. **113**, 027603 (2014).

[7] M. N. Ali, Q. Gibson, S. Jeon, B. B. Zhou, A. Yazdani, and R. J. Cava, The crystal and electronic structures of Cd_3As_2, the three-dimensional electronic analog of graphene, Inorg. Chem. **53**, 4062 (2014).

[8] Z. Wang, Y. Sun, X.-Q. Chen, C. Franchini, G. Xu, H. Weng, X. Dai, and Z. Fang, Dirac semimetal and topological phase transitions in A_3Bi (A = Na, K, Rb), Phys. Rev. B **85**, 195320 (2012).

[9] Z. K. Liu, B. Zhou, Y. Zhang, Z. J. Wang, H. M. Weng, D. Prabhakaran, S.-K. Mo, Z. X. Shen, Z. Fang, X. Dai, Z. Hussain, and Y. L. Chen, Discovery of a three-dimensional topological Dirac semimetal, Na₃Bi, Science **343**, 864 (2014).

[10] P. R. Wallace, Electronic g-factor in Cd_3As_2, Phys. Status Solidi B **92**, 49 (1979).

[11] H. Weyl, Elektron und gravitation. I., Z. Phys. **56**, 330 (1929).

[12] A. A. Burkov and L. Balents, Weyl Semimetal in a Topological Insulator Multilayer, Phys. Rev. Lett. **107**, 127205 (2011).

[13] J. W. Villanova and K. Park, Magnetic field induced Weyl semimetal from Wannier-function-based tight-binding model, Phys. Rev. B **98**, 075123 (2018).

[14] C. Zhang, Y. Zhang, X. Yuan, S. Lu, J. Zhang, A. Narayan, Y. Liu, H. Zhang, Z. Ni, R. Liu, E. S. Choi, A. Suslov, S. Sanvito, L. Pi, H.-Z. Lu, A. C. Potter, and F. Xiu, Quantum Hall effect based on Weyl orbits in Cd_3As_2, Nature **565**, 331 (2019).

[15] Y. Li and F. D. M. Haldane, Topological Nodal Cooper Pairing in Doped Weyl Metals, Phys. Rev. Lett. **120**, 067003 (2018).

[16] C. Sun, S.-P. Lee, and Y. Li, Vortices in a monopole superconducting Weyl semi-metal, arXiv:1909.04179.

[17] H. Yi, Z. Wang, C. Chen, Y. Shi, Y. Feng, A. Liang, Z. Xie, S. He, J. He, Y. Peng, X. Liu, Y. Liu, L. Zhao, G. Liu, X. Dong, J. Zhang, M. Nakatake, M. Arita, K. Shimada, H. Namatame, M. Taniguchi, Z. Xu, C. Chen, X. Dai, Z. Fang, and X. J. Zhou, Evidence of topological surface state in three-dimensional Dirac semimetal Cd_3As_2, Sci. Rep. **4**, 6106 (2014).

[18] G. A. Steigmann and J. Goodyear, The crystal structure of Cd_3As_2, Acta Crystallogr. Sect. B **24**, 1062 (1968).

[19] P. Blaha, K. Schwarz, G. K. H. Madsen, D. Kvasnicka, J. Luitz, R. Laskowski, F. Tran, and L. D. Marks, *WIEN2k: An Augmented Plane Wave plus Local Orbitals Program for Calculating Crystal Properties* (Vienna University of Technology, Vienna, Austria, 2018).

[20] J. P. Perdew, K. Burke, and M. Ernzerhof, Generalized Gradient Approximation Made Simple, Phys. Rev. Lett. **77**, 3865 (1996).

[21] R. Yu, W. Zhang, H.-J. Zhang, S.-C. Zhang, X. Dai, and Z. Fang, Quantized anomalous Hall effect in magnetic topological insulators, Science **329**, 61 (2010).

[22] C.-Zu Chang, J. Zhang, X. Feng, J. Shen, Z. Zhang, M. Guo, K. Li, Y. Ou, P. Wei, L.-L. Wang, Z.-Q. Ji, Y. Feng, S. Ji, X. Chen, J. Jia, X. Dai, Z. Fang, S.-C. Zhang, K. He, Y. Wang, L. Lu, X.-C. Ma, and Q.-K. Xue, Experimental observation of the quantum anomalous Hall effect in a magnetic topological insulator, Science **340**, 167 (2013).

[23] B. J. Wieder, Z. Wang, J. Cano, X. Dai, L. M. Schoop, B. Bradlyn, and B. A. Bernevig, Strong and fragile topological Dirac semimetals with higher-order Fermi arcs, Nat. Commun. **11**, 627 (2020).

[24] S. S. Tsirkin, I. Souza, and D. Vanderbilt, Composite Weyl nodes stabilized by screw symmetry with and without time-reversal invariance, Phys. Rev. B **96**, 045102 (2017).

[25] C. Fang, M. J. Gilbert, X. Dai, and B. A. Bernevig, Multi-Weyl Topological Semimetals Stabilized by Point Group Symmetry, Phys. Rev. Lett. **108**, 266802 (2012).

[26] G. Xu, H. Weng, Z. Wang, X. Dai, and Z. Fang, Chern Semimetal and the Quantized Anomalous Hall Effect in $HgCr_2Se_4$, Phys. Rev. Lett. **107**, 186806 (2011).

[27] This is the opposite sign convention from that adopted in Ref. [28] and some other works.

[28] D. Gosálbez-Martínez, I. Souza, and D. Vanderbilt, Chiral degeneracies and Fermi-surface Chern numbers in bcc Fe, Phys. Rev. B **92**, 085138 (2015).

[29] X. Wang, D. Vanderbilt, J. R. Yates, and I. Souza, Fermi-surface calculation of the anomalous Hall conductivity, Phys. Rev. B **76**, 195109 (2007).

[30] F. D. M. Haldane, Berry Curvature on the Fermi Surface: Anomalous Hall Effect as a Topological Fermi-Liquid Property, Phys. Rev. Lett. **93**, 206602 (2004).

[31] C. Zhang, A. Narayan, S. Lu, J. Zhang, H. Zhang, Z. Ni, X. Yuan, Y. Liu, J.-H. Park, E. Zhang, W. Wang, S. Liu, L. Cheng, L. Pi, Z. Sheng, S. Sanvito, and F. Xiu, Evolution of Weyl orbit and quantum Hall effect in Dirac semimetal Cd_3As_2, Nat. Commun. **8**, 1272 (2017).